Interferometric Synthetic Aperture Radar Phase Composition Analysis and Simulation

Zhenqiang Zhao,[1] Peng Wan,[1*] Ning Huang,[1] Chenchen Shan,[1] Zhongzheng Hu,[2] Yonghang Li,[1] and Jiafa Zhang[1]

[1]Guangzhou Marine Geological Survey, 1133 Hai Bin Road, Nansha District, Guangzhou 510075, China
[2]China Centre for Resources Satellite Data and Application,
5 Feng Xian East Road, Haidian District, Beijing 100094, China

The acquisition of data is attracting attention, and especially in the big data environment, it is important to obtain data with accurate values. The acquisition of real data is limited by the real-time changes of uncontrollable factors such as the noise of the synthetic aperture radar (SAR) sensor itself and the environment, which make the data acquired at different times slightly different and are not conducive to our experiments such as the cross-validation of data. Thus, simulated data is often used for various validation tests. On the basis of the mathematical model of interferometry synthetic aperture radar (InSAR), we can simulate the InSAR data relatively easily and the simulated data have accurate values. The study of mathematical models is the basis for the improvement of InSAR sensors. For the complex hybrid model of InSAR, in this paper, we examine the phase components of InSAR and analyze the phase models one by one. Matrix Laboratory (MATLAB) has powerful mathematical and graphical processing capabilities; thus, in this paper, we use MATLAB to simulate the data. In addition, we combine the real geographic data structure, simulation, and fusion of a region of real data to verify the feasibility of the data simulation in this paper, which provides a basis for subsequent research or InSAR sensor upgrades.

1. Introduction

Synthetic aperture radar (SAR) is a technology that achieves synthetic aperture through the forward motion of a flying platform equipped with a SAR sensor to obtain information on the backscattered signals of ground features, which is an active microwave remote sensing technology with the characteristics of all-weather, all-day operation, and has the advantage of being able to penetrate the ground surface and vegetation without atmospheric interference compared with optical sensors. SAR data are converted into backscatter coefficients using intensity characteristics that reflect the surface slope, moisture, surface roughness, and scattering mechanisms between the radar signal and objects within the resolution element. Thus,

SAR can be used for various military purposes (reconnaissance, surveillance, and targeting), vegetation monitoring, change detection, land classification, the environmental monitoring of the ocean surface, agriculture, and InSAR. The simulation of InSAR phases can not only improve our understanding of InSAR models, but also use the simulated data as true data to provide a basis for subsequent work and validation. In addition, when using InSAR for subsidence analysis in real production, we can still use the simulated phases to correct the real data to improve the accuracy of the solution. In this paper, we use MATLAB to simulate the InSAR phase in parts from the InSAR geometry model and apply it to the real data to obtain a good simulation effect.

Currently, most of the simulations for InSAR data are driven by real data. The phase is simulated from the perspective of error reduction. The best-fit planes or surfaces are utilized to attenuate the effect of satellite orbit errors. However, the phase information of other bands is ignored, making the orbit error simulation inaccurate.[1] Although the small baseline subset InSAR is effective in measuring long time-series deformations, it does not solve well the problem of errors caused by temporal correlation and other noise effects, resulting in linear variations in the interferograms.[2] Atmospheric artifacts, terrain errors, and time-series deformation measurements are estimated iteratively to reduce temporal noise and improve the quality of InSAR phase maps.[3] In addition, the digital elevation model (DEM) is transformed with super-resolution using deep learning to simulate more accurate phase maps.[4–6]

2.   InSAR Geometric Model

InSAR phase measurement involves detecting the change between two SAR data; thus, InSAR measurements usually contain both master and slave acquisitions. Data simulation is complicated by the fact that InSAR measurements are highly sensitive to terrain, ground deformation, the effects of atmospheric conditions, the spatial separation between satellites, and the nature of the ground charge. The InSAR model can be expressed as follows.[7,8] In addition, depending on the purpose of our application, part of the phase can be considered as noise.

$$\Delta\varphi = \varphi_{flat} + \varphi_{topo} + \varphi_{defo} + \varphi_{orbit} + \varphi_{atmo} + \varphi_{noise} \tag{1}$$

Here, $\Delta\varphi$ is the interferometric phase (i.e., the phase change between two acquisitions), where φ_{flat} is the horizon effect phase, φ_{topo} is the terrain phase, φ_{defo} is the phase component related to ground deformation, φ_{orbit} is the phase error caused by the orbit information error, φ_{atmo} is the atmospheric correlation phase, and φ_{noise} is the combined noise term. The geometric model of InSAR is shown in Fig. 1.

The simulated data in this paper are based on the InSAR model, which simulates the phase values of each part of InSAR. Each synthetic interferogram contains the ground level effect, surface deformation, terrain error, atmospheric errors (including ionospheric and tropospheric errors), orbit error, time decoherence, and some correlated noise. Among them, the ground level effect, surface deformation, and terrain error form the distance difference equations between two orbits, which are geometric model functions of satellite orbit and terrain.[9] Thus, the above equation can be expressed as
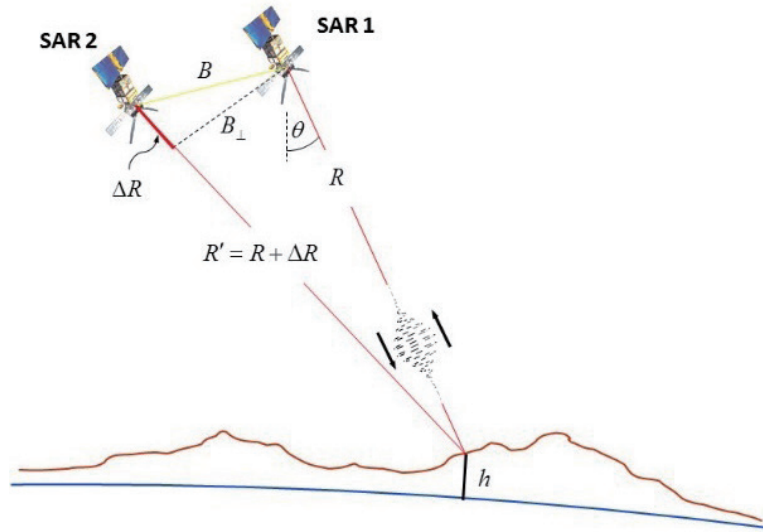
Fig. 1.   (Color online) InSAR geometric model.

$$\Delta\varphi(x,r) \approx \frac{4\pi}{\lambda}\left\{\Delta d(x,r) + \frac{B_\perp}{r\sin\theta}\Delta Z_{topo}(x,r)\right\} + \Delta\varphi_{atmo}(x,r) + \Delta\varphi_{orbit}(x,r) + \Delta\varphi_n(x,r), \quad (2)$$

where x and r are the azimuth and tilt range pixel coordinates, respectively, λ is the radar wavelength, $B_\perp$ is the vertical baseline, θ is the view angle of the SAR satellite, d is the ground displacement in the radar line of sight direction, ΔZ_{topo} is the terrain error, $\Delta\varphi_{atmo}(x,r)$ is the atmospheric error, $\Delta\varphi_{orbit}$ is the orbital baseline error, and $\Delta\varphi_n$ is the error caused by other noise sources. We will simulate the data separately in the following.

2.1   Topography phase

In the InSAR model, the topographic error is almost linearly related to the InSAR phase error, and the phase derivation process for its range change is shown in the following equation. The topographic model is shown in Fig. 2.

We can derive the relationship between the topography and the interference phase in InSAR as follows. For the flat-earth phase difference P_2,

$$\Delta\varphi_1 = \frac{4\pi}{\lambda}(R_1 - R_2). \tag{3}$$

For the phase difference P_1 with the topography h,

$$\Delta\varphi_2 = \frac{4\pi}{\lambda}B\sin(\theta - \alpha + \Delta\theta). \tag{4}$$
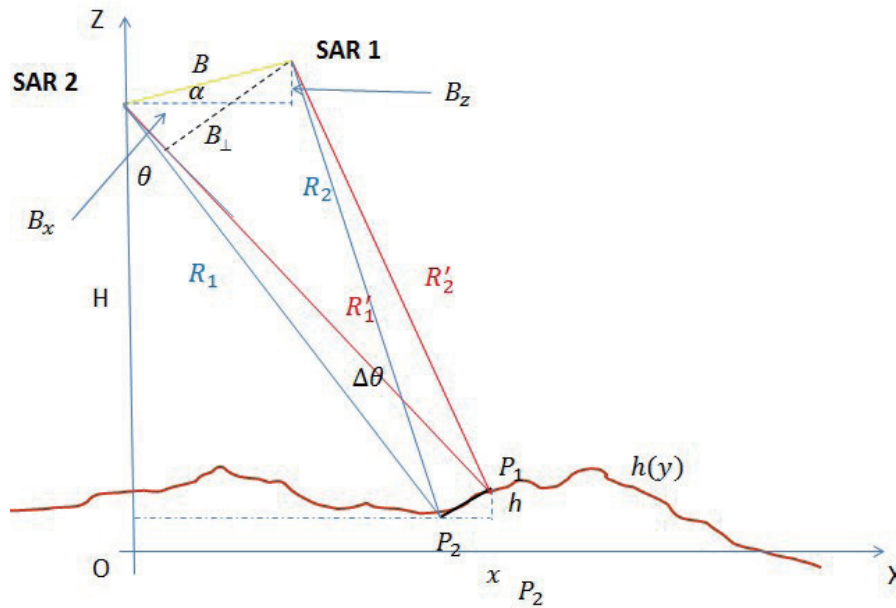
Fig. 2.   (Color online) Topographic model.

For the phase difference between $\Delta\varphi_1$ and $\Delta\varphi_2$,

$$\Delta\varphi_{topo} = \Delta\varphi_2 - \Delta\varphi_1 = \frac{4\pi}{\lambda} B \sin(\theta - \alpha + \Delta\theta) - \frac{4\pi}{\lambda} B \sin(\theta - \alpha). \tag{5}$$

Then,

$$\Delta\varphi_{topo}(x,r) = \frac{4\pi B_\perp h}{\lambda R_1 \sin\theta}. \tag{6}$$

It can be seen here that $\Delta\varphi_{topo}(x,r)$ is the topographic phase due to the topography h as well as the vertical baseline $B_\perp$. The terrain phase is referenced to the phase component of the interferogram associated with the terrain above the ellipsoid and is proportional to the vertical baseline. Thus, an interferogram with only topographic errors can be simulated from the topography h according to Eq. (6).

According to the formula, in this simulation experiment, we simulate a 512 × 512 size area with 18% of the waters (out-of-coherence part of the simulation). The simulation is shown in Fig. 3.

2.2   Flat phase

The flat ground effect refers to the phenomenon that the interferometric phase varies periodically in the distance and azimuth directions caused by the flat ground of constant height, and whether it can be removed or not will directly affect the InSAR processing and its accuracy.
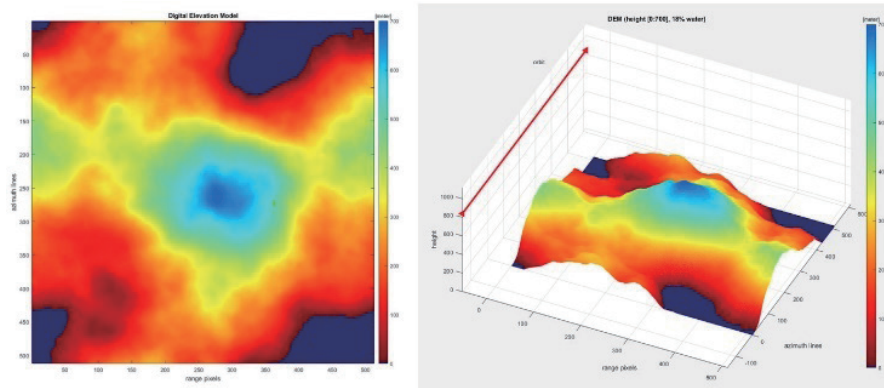
Fig. 3.   (Color online) Terrain phase simulation.

In the InSAR processing technology, the interferometric phase map can be obtained after the de-leveling effect, and this de-leveled phase map can directly reflect the terrain change. Therefore, the deplaning phase is also one of the key techniques in InSAR processing. The flat-earth effect appears as bright and dark stripes in the phase diagrams and such fringes cover the interferometric fringe changes caused by terrain changes to a certain extent. Thus, the interferometric phase map cannot directly reflect the terrain changes, which causes considerable difficulties to the phase unwinding, so the de-flat-earth effect processing must be performed before the phase unwinding processing. In the algorithm of calculating relative elevation, the accuracy of the de-leveling effect processing is one of the important factors affecting the accuracy of DEM results. The flat-earth effect is mainly affected by the height of the flight platform, the antenna pitch angle, the baseline length, and the parallelism of the flight track.[10] The horizon model is shown in Fig. 4.

As in the horizon model above, where λ is the wavelength, the phase difference at point P_1 is

$$\varphi_1 = \frac{4\pi}{\lambda} B \sin\left(\theta_0 - \alpha\right). \tag{7}$$

The phase difference at point P_2 is

$$\varphi_2 = \frac{4\pi}{\lambda} B \sin\left(\theta_0 - \alpha + \Delta\theta\right). \tag{8}$$

The phase difference between P_1 and P_2 is

$$\Delta\varphi = \frac{4\pi}{\lambda} B \left\{ \sin\left(\theta_0 - \alpha\right)\cos\Delta\theta + \cos\left(\theta_0 - \alpha\right)\sin\Delta\theta - \sin\left(\theta_0 - \alpha\right) \right\}. \tag{9}$$

Thus, the flatness effect can be expressed as

$$\Delta\varphi_{flat} = \frac{4\pi}{\lambda} * \frac{\Delta R B \cos\left(\theta - \alpha\right)\cos\theta}{R_1} \approx \frac{4\pi B_\perp \Delta R \cos\theta}{\lambda R_1}. \tag{10}$$
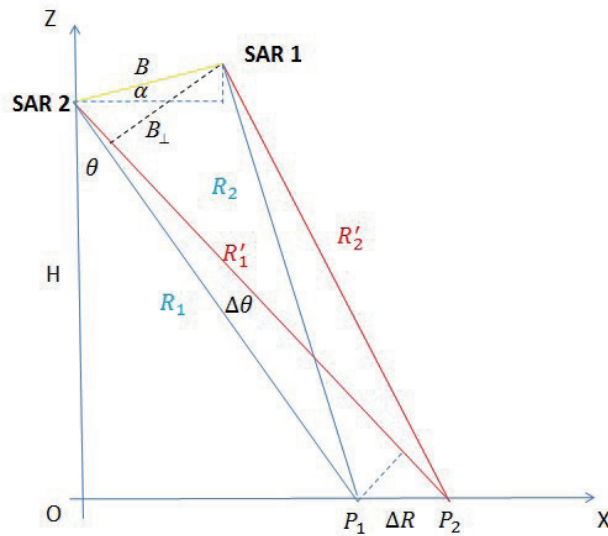
Fig. 4.   (Color online) Horizon model.

From the above equation, it is clear that even in flat earth, streaks will still form owing to the presence of ΔR. In addition, the flat-earth effect exists not only in the distance direction, but also in the azimuth direction owing to the fact that the satellite flight orbits are not perfectly parallel and Earth is an irregular ellipsoid.

The difference between the interferograms with and without the flat-earth effect is shown in Fig. 5. Figure 5(a) is a phase diagram with horizontal effects, and Fig. 5(b) is that without horizontal effects.

2.3   Deformation phase

From Eqs. (6) and (10), it is clear that both the terrain phase and the horizon effect phase are related to the baseline ($B_\perp$), which means that the terrain deformation also belongs to the geometric model related to the orbit information, so any error in the orbit information will lead to the residual phase error. As the distance between the satellite and the ground decreases, the ground behaves as a raised surface. This change in ground rise results in a negative change in phase.[11]The deformation is represented by Δr. The interferometric phase caused by the deformation is shown in Fig. 6 .

$$\varphi_{defo} = \frac{4\pi}{\lambda} \Delta r. \qquad (11)$$

Here, the InSAR phase φ_h consists of a topographic φ_{topo} component (dependent on the elevation H and baseline B) and a deformation component (differential).

(a)   (b)
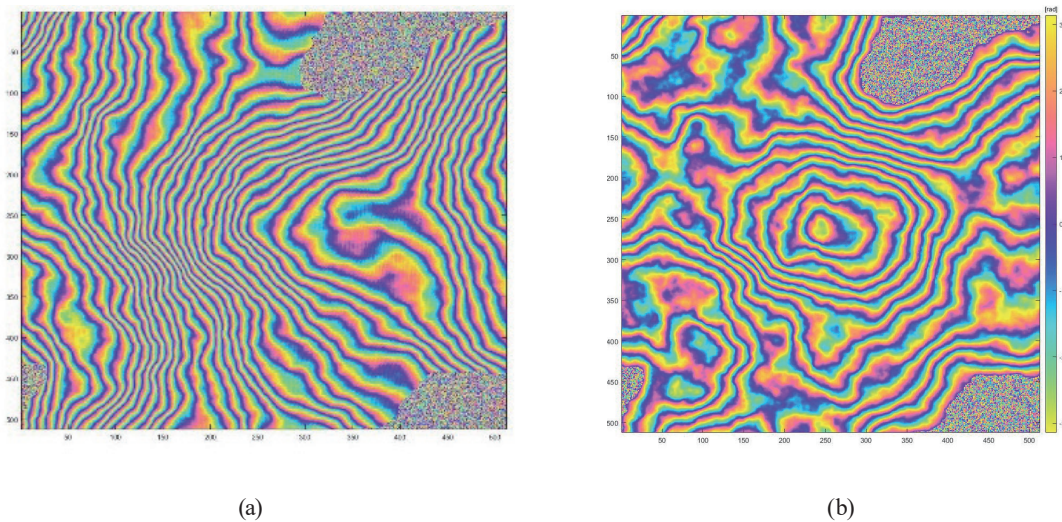
Fig. 5.   (Color online) Flat phase simulation. (a) Phase diagram with horizontal effects. (b) Phase diagram without horizontal effects.
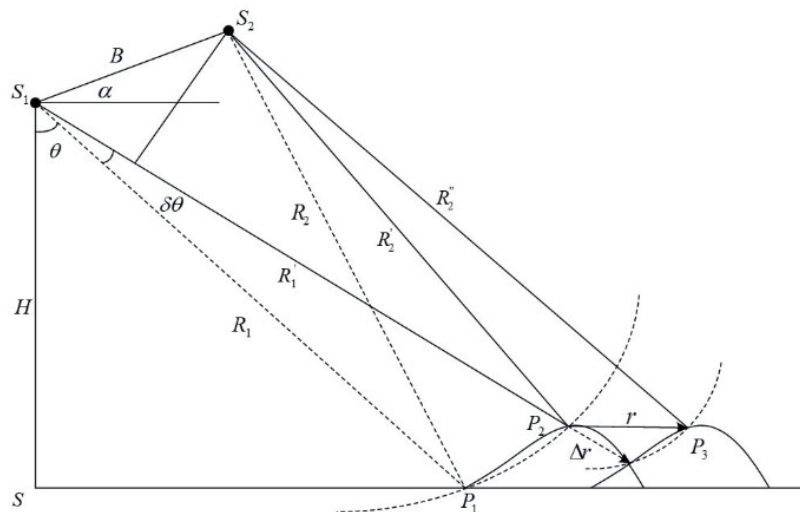

Fig. 6.   Deformation model.

2.4   Orbital phase

An important source of error in InSAR deformation measurements is the inaccurate SAR antenna position, and the resulting baseline error makes the measurement inaccurate. In the InSAR processing, orbital parameters are generally not used directly, but accurate orbital data after re-estimation calculation are used. Even after the satellite's orbit is precisely corrected, baseline errors can occur in the interferogram. For example, ERS-1 and ERS-2 can have precisely corrected orbital errors up to about 7 cm radially and about 18 cm laterally when using

the Delft gravity model. The interferometric baseline error for ERS-1/2 is about 27 cm, calculated as $\sqrt{2}$ times the satellite position error (about 19 cm).[12–14] Given the system parameters of ERS-1/ERS-2, the difference in phase error from the near range to the far range is about 2.3π radians, which corresponds to a surface deformation of about 3.3 cm. The interferogram phase error due to the baseline error is modeled in this paper using a first-order polynomial.

$$\Delta\varphi_{orbit}(x, y) = ax + br + c \tag{12}$$

Here, a and b are the gradient parameters in the distance (r) and azimuth (x) directions, respectively, and c is the offset parameter. On the basis of the phase distortion of the typical baseline error of the ERS system, we allow a maximum phase distortion within the InSAR image of about 4 cm. For each interferogram, the random parameters a, b, and c in the above equation are estimated and used for this orbital error simulation, and the orbital error phase components are first-order-correlated as shown in Fig. 7.

2.5 Atmospheric phase

Like other astronomical and space geodetic techniques, InSAR measurement techniques are also affected by the atmosphere, especially atmospheric water vapor, and according to the available research results, the atmospheric effects (especially the effect of atmospheric water vapor) make the application of InSAR techniques for surface deformation monitoring very limited, especially when the surface deformation variables are relatively small.[15–19] Therefore, the effect of the atmosphere must be studied, analyzed, and dealt with in the InSAR data processing and interpretation of interferometric images.

Changes in atmospheric conditions during the acquisition of master and slave images can also affect interferometric phase measurements. The phase component that affects the troposphere comes from the fact that the refractive index of the troposphere is slightly higher than that of free space, and that tropospheric phase delays can be divided into wet and dry components, which are usually included in the phase cycle.
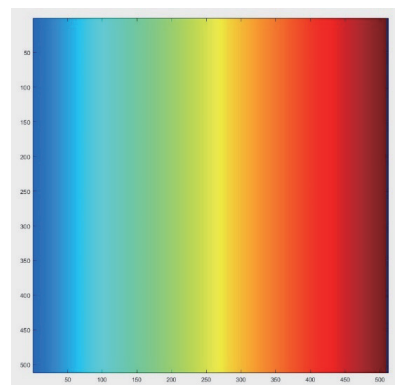

Fig. 7.   (Color online) Orbital phase simulation.

$$\varphi_{tropo} = \frac{4\pi}{\lambda} \Delta R_{tropo} \tag{13}$$

Here, ΔR_{tropo} indicates the range variation due to atmospheric delay. The atmospheric phase fraction can be estimated using a number of models. In general, the tropospheric phase component is referred to as the atmospheric phase screen for the C-band radar; however, for the L-band radar, variations in the total electron content (TEC) of the ionosphere can affect the interferometric phase. Random variations in ionospheric conditions can cause satellite distances and azimuths to blur, making the image alignment difficult, while image coherence may be reduced by Faraday rotation. A 1 unit difference in TEC (10^{16} m^{-2}) will result in a phase delay of 2 cycles for the L-band, 0.5 cycles for the C-band, and 0.3 cycles for the X-band, given by

$$\varphi_{iono} = 1.69 \times 10^{-16} N\lambda, \tag{14}$$

where N is the number of electrons per unit area and λ is the wavelength. On the basis of the above equation, we simulate the atmospheric phase diagram for the region as shown in Fig. 8.

2.6   Combined error terms

Before introducing the combined noise term φ_{noise}, we need to understand the interferometric phase image coherence, which is often used to describe the good or bad quality of interferometric maps. The interferogram coherence is defined as the complex correlation between the main image and the acquisition from the image. The loss of coherence effect or excessive noise can reduce the coherence γ of the interferogram.

The coherence value can be related to the expected variance of the InSAR phase measurements,[20] so that the combined phase noise φ_{noise} can be described as
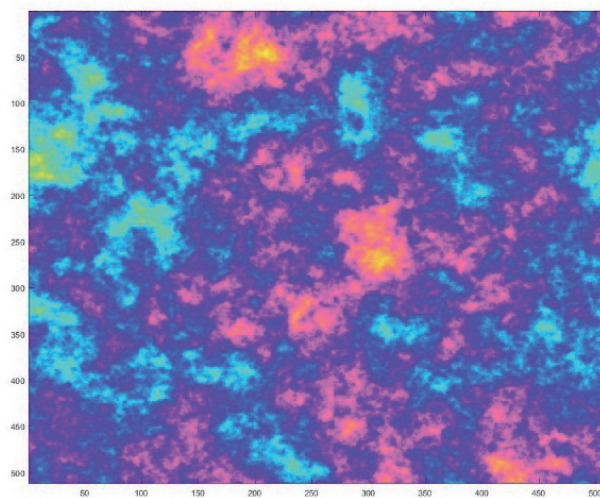

Fig. 8.   (Color online) Atmospheric phase simulation.

$$\sigma^2_{\varphi_{noise}} = \int_{-\pi}^{\pi} \varphi^2_{noise} pdf \left(\varphi_{noise} \right) d\varphi_{noise}, \tag{15}$$

where $\sigma^2_{\varphi_{noise}}$ is the expected phase variance, φ_{noise} is the integral variable over $[-\pi, \pi]$, and $pdf(\varphi_{noise})$ is the probability density function of the phase deviation of φ_{noise}, and this probability density function is defined as

$$pdf \left(\varphi_{noise} \right) = \frac{1 - |\gamma|^2}{2\pi} \times \frac{1}{1 - |\gamma|^2 \cos^2 \left(\varphi_{noise} \right)} \times \left(1 + \frac{|\gamma| \cos(\varphi_{noise}) \arccos \left[-|\gamma| \cos(\varphi_{noise}) \right]}{\left[1 - |\gamma|^2 \cos^2 \left(\varphi_{noise} \right) \right]^{1/2}} \right). \tag{16}$$

Here, γ refers to coherence, which is the only parameter for calculating a certain determined integrated phase noise density function.

The interfering phase-integrated noise term φ_{noise} can be associated with coherence and divided into four different de-correlation terms.[21] In addition, the effects of the different decoherence terms are independent of each other and can be expressed as

$$\gamma_{total} = \gamma_{spatial} \times \gamma_{Doppler} \times \gamma_{temporal} \times \gamma_{thermal}, \tag{17}$$

where γ_{total} denotes the total interferometric coherence term, $\gamma_{spatial}$ is the spatial baseline out-of-correlation, $\gamma_{temporal}$ is the temporal out-of-correlation, $\gamma_{Doppler}$ is the Doppler center out-of-correlation, and $\gamma_{thermal}$ is the sensor heat out-of-correlation.

If the two images are correlated, the correlation γ_{total} is 1. The spatial baseline uncorrelation is related to the horizontal separation between the two satellite orbits; thus,

$$\gamma_{spatial} = 1 - \frac{2|B_h| S_{range} \cos^2 \theta}{\lambda R}, \tag{18}$$

where B_h is the horizontal baseline, S_{range} is the distance resolution, θ is the angle of view, and R is the satellite distance. When the image is completely out of coherence, $\gamma_{spatial}$ becomes zero, and the baseline B_h at this moment is the critical baseline B_c.

The Doppler-centered out-of-correlation effect may occur when the attitude (yaw, roll, and pitch) of the satellite is not synchronized during the primary and secondary image acquisitions. This effect is caused by the presence of the oblique viewing angle (Ψ), which depends on the yaw and pitch of the satellite.[22]

A satellite-based Cartesian coordinate system is provided as in Fig. 9 across the orbital and radial altitude axes. θ is the angle of view and Ψ is the oblique angle of view. The rotation along the direction of flight (z-axis) is roll, that about the collateral direction (x-axis) is pitch, and that about the y-axis is yaw.[23]

Figure 9 demonstrates the geometric imaging and viewing angle relationships involved. The Doppler decorrelation $\gamma_{Doppler}$ is determined on the basis of the tilt angle of view as well as the distance resolution.
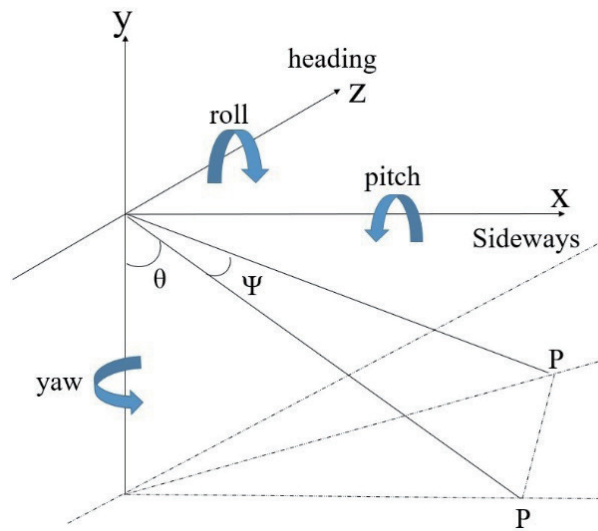
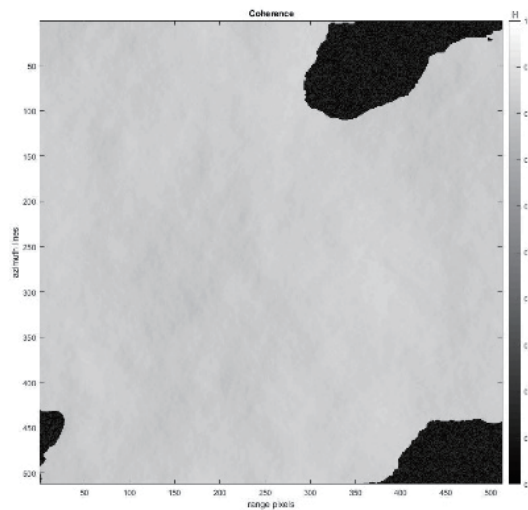Fig. 9.   (Color online) Satellite attitude.

Fig. 10.   (Color online) Coherence simulation.

$$\gamma_{Doppler} = 1 - \frac{2\sin\theta \left| \Delta\Psi \right| S_{range}}{\lambda} \tag{19}$$

Here, θ is the viewing angle, $\Delta\Psi$ is the variation of the primary and secondary images with respect to the oblique viewing angle, and S_{range} is the distance resolution.

When the physical properties of the scatterers in the resolution cell change with time, the temporal decoherence $\gamma_{temporal}$ occurs. When the interferometric region is dominated by ecological regions such as grasses and waters, the effect of $\gamma_{temporal}$ is stronger. In addition, the

<div align="center">(a)   (b)</div>
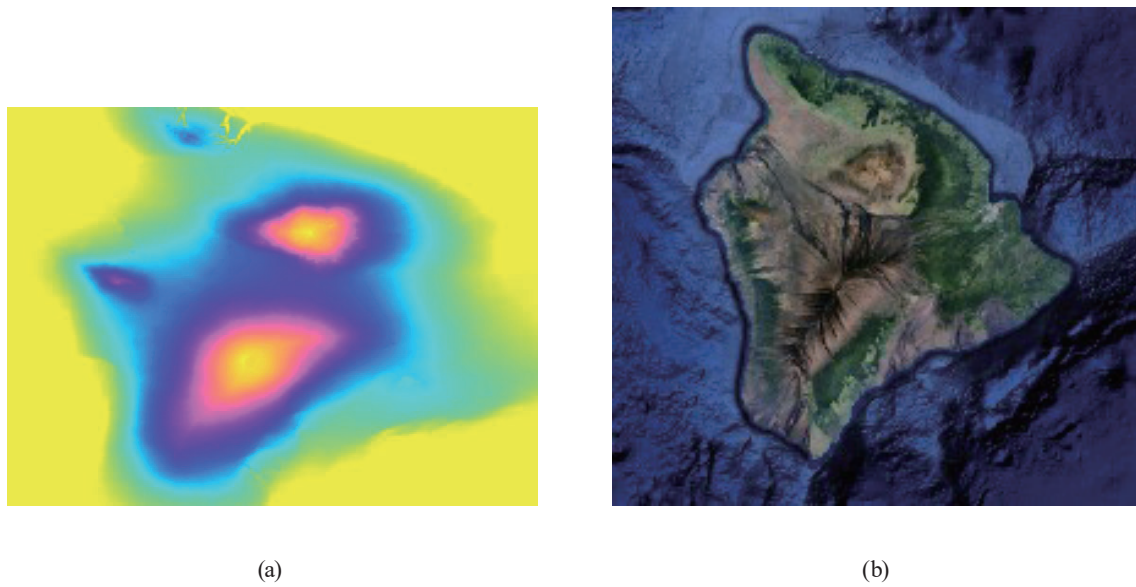
Fig. 11.   (Color online) Real data terrain (Hawaii Island, USA). (a) DEM and (b) remote sensing image.
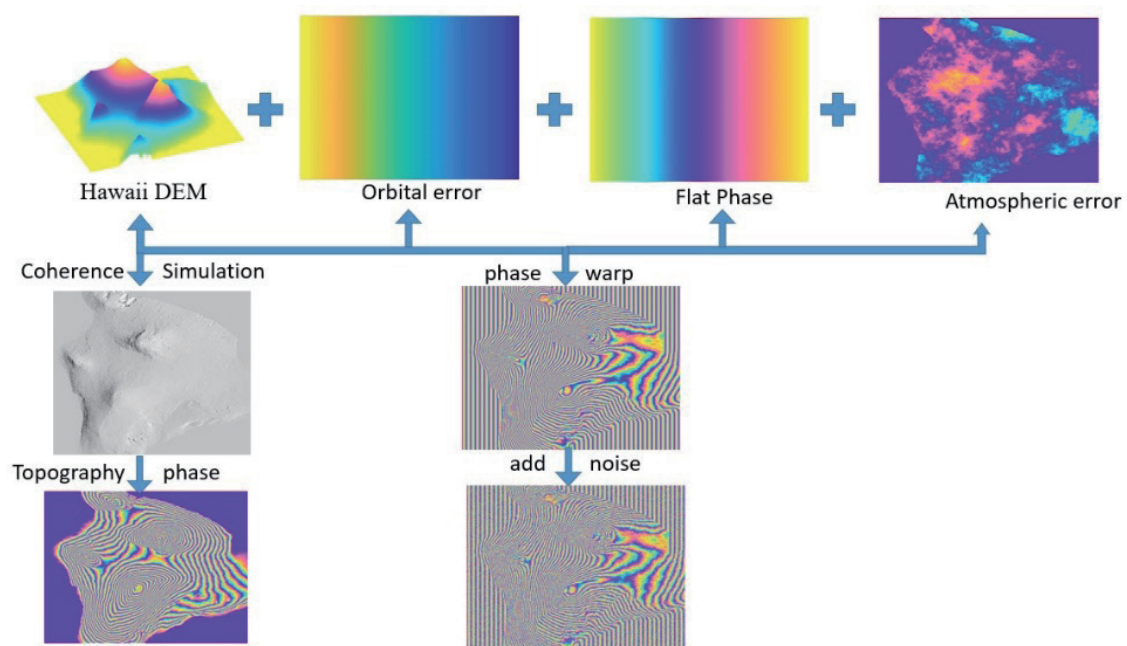

Fig. 12.   (Color online) Comprehensive mockup.

thermal noise of the radar also generates a decoherence term $\gamma_{thermal}$, which is usually neglected in the interferometric measurements. The simulated data in this paper have the following coherence relations, which can be seen in the corner water part of the basic out-of-coherence. The coherence simulation is shown in Fig. 10.

3.   Real Data Experiments

On the basis of the previous sections of this paper, combined with the real data, it is possible to simulate composite data with similar master and slave images in this study; the master image is shown in Fig. 11. The real data were selected from the island of Hawaii, which is the largest island in the Hawaiian archipelago, which is also known as Big Island. It is located at the southernmost point of the archipelago and has an area of 10414 km^2. The island is rich in volcanic activity, and there are five shield volcanoes on the island, including Bold Naroya, which is 4170 meters above sea level and is a world-famous active volcano with a large vent of 5 km diameter and often emits lava. The DEM is shown in Fig. 11(a) and the remote sensing image is shown in Fig. 11(b).

The phase synthesis of each part of the region is shown in Fig. 12. The above real phase simulation can be used in de-leveling effect algorithm research, phase decoupling algorithm research, atmospheric effect on SAR phase research, and the real production of subsidence correction to improve accuracy.

4.   Conclusion

In this study, we solved the problems of difficult access to real data and the uncontrollable quality of SAR sensors through data simulation. The inaccuracy of the data is not conducive for conducting subsequent research requiring data-based studies. In this study, the InSAR phase fraction is formulated according to the InSAR geometric model, each part of the phase is simulated according to the formula, and the data can be applied to the study of the InSAR phase decoupling algorithm to provide real values for the decoupling algorithm. In the context of big data, the simulated data can also provide a large amount of data basis for the study of the deep learning algorithm. In addition, the simulation algorithm in this paper can also be used for real data experiments, and the phase simulation map of the region can be simulated according to the regional DEM, which can provide a reference basis for subsequent realistic applications such as subsidence.

In addition, the atmospheric model used for data simulation in this paper is not universal and needs to be adapted for different regions in the future, and the real data simulation does not incorporate the part of terrain change, so it needs to be analyzed over a long period of time in the future to further simulate more realistic data and provide a reliable database for solving real problems.

References

1   R. F. Hanssen: Radar Interferometry Data Interpretation and Error Analysis (Springer, Dordrecht, 2001). https://doi.org/10.1007/0-306-47633-9

2   P. Berardino, G. Fornaro, R. Lanari, and E. Sansosti: IEEE Trans. Geoscience and Remote Sensing **40** (2002) 2375. https://doi.org/10.1109/TGRS.2002.803792

3   D. A. Schmidt and R. Buergmann: J. Geophys. Res. **108** (2003) 2416. https://doi.org/10.1029/2002JB002267

4   X. Zekai, C. Zixuan, Y. Weiwei, G. Qiuling, W. Hou, and D. Mingyue: ISPRS J. Photogramm. Remote Sens. **150** (2019) 80. https://doi.org/10.1016/j.isprsjprs.2019.02.008

5   B. Z. Demiray, M. Sit, and I. Demir: arXiv (2020) 2004.04788. https://doi.org/10.48550/arxiv.2004.04788

6   C. Ledig, L. Theis, F. Huszar, J. Caballero, A. Cunningham, A. Acosta, A. Aitken, A. Tejani, J. Totz, Z. Wang, and W. Shi: arXiv (2016) 1609.04802. https://doi.org/10.48550/arxiv.1609.04802

7   C. Colesanti, A. Ferretti, F. Novali and C. Prati: IEEE Trans. Geoscience and Remote Sens. **41** (2003) 1685. https://doi.org/10.1109/TGRS.2003.813278

8   A. Ferretti, C. Prati, and F. Rocca: IEEE Trans. Geoscience and Remote Sens. **39** (2001) 8. https://doi.org/10.1109/36.898661

9   P. A. Rosen, S. Hensley, I. R. Joughin, F. K. Li, S. N. Madsen, E. Rodriguez, and R. M. Goldstein: Proc. IEEE **88** (2002) 333. https://doi.org/10.1109/5.838084

10 D. Carrasco, J .Alonso, and A. Broquetas: 1995 Int. Geoscience and Remote Sensing Symposium (1995) 781. https://doi.org/10.1109/IGARSS.1995.520584

11 A. Ferretti, A. Monti-Guarnieri, C. Prati, F. Rocca, and D. Massonet: Informs Trans. Educ. **10** (2007) 103. https://doi.org/10.1287/ited.1100.0047

12 A. O. Kohlhase, K. L. Feigl, and D. Massonnet: J. Geodesy **77** (2003) 493. https://doi.org/10.1007/s00190-003-0336-3

13 J. Sang and J. C. Bennett: Adv. Space Res. **54** (2014) 119. https://doi.org/10.1016/j.asr.2014.03.012

14 R. Scharroo and P. Visser: J. Geophysical Res. Oceans **103** (1998) 8113. https://doi.org/10.1029/97JC03179

15 S. F. M. Ashbourn, M. E .Jenkin, and K. C. Clemitshaw: J. Atmos. Chem. **29** (1998) 233. https://doi.org/10.1023/A:1005992316512

16 A. Bonforte, A. Ferretti, C. Prati, G. Puglisi, and F. Rocca: J. Atmos. Solar-Terrestrial Phys. **63** (2001) 1343. https://doi.org/10.1016/S1364-6826(00)00252-2

17 D. B. Crosetto: Real Time Conf. (1999). https://doi.org/10.1109/RTCON.1999.842634

18 D. L. Fried: J. Optical Soc. Am. **67** (1977) 370. https://doi.org/10.1364/JOSA.67.000370

19 D. Just and R. Bamler: Appl. Optics **33** (1994) 4361. https://doi.org/10.1364/AO.33.004361

20 H. A. Zebker and J .Villasenor: IEEE Trans. Geoscience and Remote Sens. **30** (2002) 950. https://doi.org/10.1109/36.175330

21 N. Mir, B. Rosich, C. Santella, and M. Grion: Int. J. Engineering Sci. **43** (2013) 721. https://doi.org/10.1016/j.ijengsci.2004.12.011

22 Z. Li, E. J. Fielding, and P. Cross: IEEE Trans. Geoscience and Remote Sens. **47** (2009) 3220. https://doi.org/10.1109/TGRS.2009.2019125

23 O. Loffeld and R. Kramer: IEEE Trans. Geoscience Remote Sens. **46** (2007) 47. https://doi.org/10.1109/TGRS.2007.909081